Flow transitions in two-dimensional foams

Christopher Gilbreth, Scott Sullivan, and Michael Dennin
Department of Physics and Astronomy, University of California at Irvine, Irvine, California 92697-4575, USA
(Received 8 August 2006; published 21 November 2006)

For sufficiently slow rates of strain, flowing foam can exhibit inhomogeneous flows. The nature of these flows is an area of active study in both two-dimensional model foams and three dimensional foam. Recent work in three-dimensional foam has identified three distinct regimes of flow [S. Rodts, J. C. Baudez, and P. Coussot, Europhys. Lett. **69**, 636 (2005)]. Two of these regimes are identified with continuum behavior (full flow and shear banding), and the third regime is identified as a discrete regime exhibiting extreme localization. In this paper, the discrete regime is studied in more detail using a model two-dimensional foam: a bubble raft. We characterize the behavior of the bubble raft subjected to a constant rate of strain as a function of time, system size, and applied rate of strain. We observe localized flow that is consistent with the coexistence of a power-law fluid with rigid-body rotation. As a function of applied rate of strain, there is a transition from a continuum description of the flow to discrete flow when the thickness of the flow region is approximately ten bubbles. This occurs at an applied rotation rate of approximately 0.07 s^{-1}.

DOI: 10.1103/PhysRevE.74.051406 PACS number(s): 83.80.Iz, 83.10.Gr, 64.70.Pf

I. INTRODUCTION

Nonlinear viscoelastic materials are observed to exhibit inhomogeneous flows. One source of inhomogeneous flow is geometric. When subjected to certain boundary conditions, an inhomogeneous stress will be applied to the fluid, resulting in an inhomogeneous flow. A classic example is a yield stress fluid in a Couette geometry (flow between concentric cylinders). A yield stress fluid only flows if the stress is above a critical stress, and in a Couette geometry, the stress decreases as a function of the radial distance from the inner cylinder. Therefore, it is possible to generate flow close to the inner cylinder where the stress is above the yield stress, and at the same time, there will be no flow beyond a critical radius. The critical radius corresponds to the point at which the stress has decreased below the yield stress [1]. Though inhomogeneous flows are not a new phenomenon, it has been challenging to directly measure them due to the inherent opacity of most complex fluids, such as foams, granular matter, colloids, emulsions, pastes, etc. Direct measurements of such flows have focused on two-dimensional systems [2,3] (for which the entire material is observable) and nonoptical techniques in three-dimensional systems, such as MRI techniques [4]. A surprising element of these direct studies of velocity profiles is the observation of inhomogeneous flow that cannot be understood in terms of the geometry and the resulting stress distribution.

Direct measurement of velocity profiles has covered a range of diverse systems. These include wormlike micelles [5,6], lyotropic lamellar phases [7,8], granular matter [9–11], slurries and pastes [4,12], and foams [2,3,13–16]. In most of these studies, inhomogeneous flows take the form of *flow localization* or *shear localization*. This refers to the fact that the system divides into two spatial regions: a flowing region and a stationary (or solidlike) region. The breadth of systems exhibiting this general behavior naturally leads to questions of universality of the observed flow localization.

One issue with the universality of flow localization is the nature of the transition from the flowing to the stationary region. At this transition, the rate of strain has been observed to be either continuous or discontinuous. In continuous transitions, the rate of strain is continuous as the system makes the transition from flow to no flow. For this class of behavior, the velocity as a function of position in the system is often well fit by an exponential [2,10]. Such continuous behavior was the first class of inhomogeneous flows that was identified as potentially universal across different systems, having been observed in both granular and foam systems. Though not central to the work in this paper, it is worth noting that in granular matter, the velocity profile has been attributed to a spatial variation in the density that develops during flow [10]. This results in a spatial variation of the viscosity that is the source of the shear localization. For foam, exponential profiles were observed in foam confined in a Hele-Shaw cell [2]. However, experiments [17] and simulation [18] suggest that this type of continuous transition is caused by drag due to the confining plates.

More recently, experiments have identified examples of discontinuous transitions. Such flows have been observed in various slurries and pastes [4,12], including three-dimensional foam [16], in two-dimensional model foams known as bubble rafts [3], and in wormlike micelles [5] and lyotropic lamellar systems [7]. In these flows, the rate of strain is discontinuous across the system, often at a transition from shear flow to rigid-body-type behavior. Discontinuous flows have not yet been observed in simulations, though a number of simulations exhibit continuous flow localization [18–22].

The above discussion assumes that the materials are well described by a continuum model through the selection of a specific constitutive relation. For the case of flow in a three-dimensional foam, there has been a detailed study of the flow behavior that combines standard rheological measures of stress with direct measurement of velocity profiles using a Couette geometry [16]. For these studies, a large system size

was used that allowed for the categorization of the flow into two classes. When the width of the flowing region is above a critical value, a single constitutive relation that is based on the existence of a critical rate of strain is used to describe the flow of the foam over a wide range of rates of strain. This is to be expected in the continuum limit. When the width of the flowing region is less than a critical value, a different type of behavior is observed. This has been called the "discrete flow" regime.

The discrete regime was observed to occur when the flow is localized to a spatial width that is less than approximately 25 bubble diameters. This corresponded to a critical rotation rate for the driving cylinder (in this case the inner cylinder) on the order of 0.3 s^{-1} [16]. For the discrete regime, there does not exist a single continuum model that describes all of the flow curves. For example, when the system is driven by rotating the inner cylinder with a constant rotation rate, the torque as a function of the applied rotation rate does not follow a well-defined curve.

Previous measurements on a bubble raft suggest that the discrete regime occurs in two-dimensional foam as well [3]. A bubble raft consists of a single layer of bubbles floating on the water surface [23,24]. Studies of the flow behavior of a bubble raft using a Couette geometry demonstrated the coexistence of flowing and nonflowing regions with a rate of strain discontinuity between the two regions [3]. In these studies, constant rotation of the outer cylinder was used to generate the flow. Two different external rotation rates were studied, and in both cases, the velocity profile in the flowing region was well described by a power-law fluid. However, different power-law fluid models were required for each case. Because the total system size was only 25–30 bubbles across, this is consistent with the expectation of a discrete flow regime. The possible connection between these flows and the observed discrete regime in three-dimensional fluids provided the motivation for the study reported on in this paper. A critical question in the flow of complex fluids is the dependence of the behavior on dimensionality. Therefore, a detailed understanding of the discrete to continuum transition is needed in the two-dimensional system.

In this paper, we report on a more complete study of the flow in the small-system-size bubble raft to elucidate *both* the nature of the solid to fluid transition (i.e., whether it is continuous or discontinuous) *and* to determine if there is a transition from the continuum limit to discrete flow. We focused on low rates of strain and considered two different system sizes. We use a foam confined between two cylinders and apply a constant rate of rotation of the outer cylinder. We confirm the existence of a transition between a discrete flow regime and a continuum limit as a function of the rotation rate of the outer cylinder. In both cases, the flow can be described as the coexistence of a power-law-type fluid and a rigid body, with a discontinuity in the rate of strain. However, in the discrete regime, one cannot use a single, consistent power-law model for all rotation rates. The rest of the paper is organized as follows. Section II describes the experimental setup and techniques. Section III discusses the models used to describe the data, and Sec. IV presents the results. Section V is a discussion of the results.

II. EXPERIMENTAL METHODS

The experimental system consisted of a standard bubble raft [24] in a Couette geometry (two concentric cylinders). The system was driven by rotating the outer cylinder at a constant angular speed. Stress measurements were made using the inner cylinder, which was suspended on a torsion pendulum. The studies used two values of the outer radius (R): 7 cm and 9 cm. The inner cylinder had a fixed radius of $r_i=2.85$ cm. The bubble raft was produced by flowing regulated nitrogen gas through a hypodermic needle into a homogeneous solution of 80% by volume de-ionized water, 15% by volume glycerine, and 5.0% by volume Miracle Bubbles (Imperial Toy Corp.). The bubble size was dependent on the nitrogen flow rate, which was varied using a needle valve. A random distribution of bubble sizes was used, with an average radius of 1.7 mm and 15–22 bubbles across, depending on the outer radius. In previous versions of this system, the bubbles were generated separately and transferred into the apparatus. For these experiments, the bubbles were generated directly in the Couette apparatus. For each setting of the outer radius, essentially the same set of bubbles were used. Occasionally, near the end of a run, some bubbles would pop. Data were only used up to the point the first bubbles were observed to pop, and the bubble raft was filled in before the next run. For additional details of the apparatus, see Ref. [25].

As mentioned, the system was driven by rotating the outer cylinder at a constant angular velocity Ω. The range of angular speeds used was $0.01\ s^{-1} \leqslant \Omega \leqslant 0.35\ s^{-1}$. The first layer of bubbles at either boundary was not observed to slip relative to the boundary. At the outer boundary, this was due to the curvature of the boundary. At the inner boundary the first layer of bubbles was held in place with metal fins attached to the boundary. Due to the finite size of the bubbles, this resulted in an effective inner radius on the order of 3.1–3.2 cm, depending on the details of the system.

As the experiments focus on the average velocity profile and the corresponding rate of strain (or shear rate) as a function of radial position, it is useful to review what is expected for Newtonian fluids in a Couette geometry. Due to the cylindrical geometry, the shear rate is not necessarily uniform across the system and is given by $\dot{\gamma}(r)=r\frac{d}{dr}\frac{v_\theta(r)}{r}$. Here v_θ is the azimuthal velocity of the bubbles. Because we rotate the outer cylinder, it is useful to normalize the velocity by the expected velocity for rigid-body rotation $V(r)=\Omega r$, where r is the radial position of interest. Therefore, we will often refer to the scaled azimuthal velocity $v(r)=v_\theta(r)/\Omega r$. It should be noted that because we rotate the outer cylinder, the bubbles in the outer portion always move. Therefore, with our setup, what distinguishes the "flowing" region from the "solid" region is the type of motion. The solid region exhibits rigid-body rotation and has $v(r)=1$. This is in contrast to many experiments in which the inner cylinder drives the system and "solid" behavior corresponds to a zero velocity for bubbles in the outer portion of the system.

To measure the velocity, roughly one-third of the trough was digitally recorded using a frame grabber. The time interval between images was selected so that the fastest-moving

bubbles could be accurately tracked from frame to frame. The radial coordinate is divided into bins of width 0.15 cm and 0.18 cm for the 7-cm and 9-cm data, respectively. This represents roughly an average bubble radius per bin. The details of the velocity measurements are given in Ref. [3].

III. MODELS

From previous stress versus rate of strain studies [26] and measurements based on step-strains [27], it is clear that the bubble raft possesses a yield stress. However, the open question is how best to describe the flow of the system at low rates of strain. Because the flow is localized, the velocity profile is not necessarily related in any simple way to the global stress as a function of rate of strain measurements. In fact, in the regime of slow flow, the global stress, as measured on the inner cylinder, is essentially equal to the yield stress. Given this, the goal of fitting the flow data is to better understand the local flow behavior of the system and not to determine a "correct" global constitutive relation. To accomplish this, the data reported in Sec. IV will be discussed in the context of two standard continuum models for non-Newtonian fluids: the Herschel-Bulkley model and power-law fluid model [28]. By fitting the data to these two models, we gain insight into whether or not the transition from fluidlike to solidlike behavior is continuous or discontinuous in the rate of strain and into whether or not there is a transition from continuum to discrete flow. We can address the first question, because by construction, the Herschel-Bulkley model is continuous in the rate of strain and the power-law model allows for a rate of strain discontinuity. We will show that the power-law model, with a rate of strain discontinuity, is the more consistent with the data. Once this is established, the power-law model provides an effective method of characterizing the transition from the continuum limit to the discrete flow regime. In this section, we review the main elements of each model that are used to analyze the data. The details of the derivations are left to the Appendix, as indicated.

The key element of the Herschel-Bulkley model is the yield stress τ_0. If the stress is below the yield stress, the material acts as a solid. For stresses above the yield stress, the material obeys the following constitutive relation for the average stress σ as a function the of rate of strain $\dot{\gamma}$ [28]:

$$\sigma(\dot{\gamma}) = \tau_0 + \mu\dot{\gamma}^n. \tag{1}$$

As one can see, this model is explicitly continuous in the rate of strain. Also, it is important to point out that it provides a good fit to previous measurements of stress versus rate of strain in bubble rafts. Some typical values for a bubble raft are $\tau_0 = 0.8 \pm 0.1$ mN/m and $n = 0.33$ [3,26]. Second, the model has a built-in physical mechanism for the transition from solidlike behavior to flow: the yield stress. In general, the value of the radial position at which the transition from solidlike to fluidlike behavior occurs is the critical radius r_c. In the Herschel-Bulkley model, r_c is determined by equating $\sigma(r)$ with τ_0.

The second model was selected based on previous velocity profiles [3] and MRI measurements of velocity profiles in three-dimensional foam [16]. These experiments suggest that the system is best described by a power-law fluid coexisting with the elastic solid regime. For a generic power-law fluid,

$$\sigma(\dot{\gamma}) = \mu\dot{\gamma}^n. \tag{2}$$

In this case, there is no specification of where the fluid-solid transition will occur. To account for this, a modified power-law fluid that explicitly includes a critical rate of strain ($\dot{\gamma}_c$) was introduced in Ref. [16]:

$$\sigma(\dot{\gamma}) = \mu(\dot{\gamma}/\dot{\gamma}_c)^n \quad \text{for } \dot{\gamma} > \dot{\gamma}_c, \tag{3}$$

for $\dot{\gamma} < \dot{\gamma}_c$, $\dot{\gamma} = 0$. Notice that this is fundamentally different from the Herschel-Bulkley model in which r_c is set by a critical stress. For this power-law model, r_c is determined by $\dot{\gamma}_c$ and there is a built-in discontinuity in $\dot{\gamma}$ at r_c. Localized flow occurs when there is a coexistence of a flowing region for $r < r_c$ (where $\dot{\gamma} > \dot{\gamma}_c$) and a "solid" region for $r > r_c$ (where $\dot{\gamma} = 0$).

Independent of the model, the stress in a Couette geometry has the form $\sigma(r) = C/r^2$, where the constant C is determined by the boundary conditions (either at the inner cylinder or r_c, whichever is more convenient). Combining this relation with the particular constitutive model allows one to solve for $v(r) \equiv v_\theta/\Omega r$. This in turn can be fit to the velocity data as a test for each model. For the Herschel-Bulkley model, we get, for $r \leqslant r_c$,

$$v(r) = \frac{1}{N}\int_{r_i}^{r} \frac{1}{\rho}\left[\left(\frac{r_c}{\rho}\right)^2 - 1\right]^{1/n} d\rho, \tag{4}$$

where

$$N = \int_{r_i}^{r_c} \frac{1}{\rho}\left[\left(\frac{r_c}{\rho}\right)^2 - 1\right]^{1/n} d\rho.$$

For $r \geqslant r_c$, the solid-body behavior gives $v = 1$; adjoining the solutions for $r \leqslant r_c$ and $r \geqslant r_c$ yields a smooth curve where the fit parameters are the exponent n, r_i, and r_c. For the power-law case, we find

$$v(r) = \frac{A}{r^{2/n}} - B. \tag{5}$$

Applying the same boundary conditions as before, $A = (r_i r_c)^{2/n}/(r_i^{2/n} - r_c^{2/n})$ and $B = r_c^{2/n}/(r_i^{2/n} - r_c^{2/n})$. In this case, because of the rate of strain discontinuity, a smooth continuation of the power-law solution and the solid-body curve does not exist. Therefore, the data in the range $0.25 < v < 0.95$ are fit to Eq. (5) with n, r_i, and r_c as fit parameters. Equivalently, r_c can be computed as the intersection the line $v = 1$ ($v_\theta = \Omega r$) with a fit to Eq. (5) with A, B, and n as free parameters. Notice that $\dot{\gamma}_c$ is not a fit parameter, as it does not appear in the solution for the power-law model. To determine $\dot{\gamma}_c$, one uses the resulting fit and computes $\dot{\gamma}(r_c)$.

In terms of testing the models for their applicability, it is important to note a few similarities and differences. In both models the three main fit parameters are n, r_i, and r_c. The determination of r_c and r_i provides a consistency check, as both (within a few percent) are relatively easy to determine by visual inspection of the data, independent of the selected

model. Therefore, one does not expect to be able to distinguish the models on this basis. On the other hand, n has definite physical meaning. It gives the scaling of the stress (or the effective viscosity) as a function of rate of strain. For $n<1$, the material acts as a shear thinning material. For $n>1$, the material acts as a shear thickening material. All of the measurements of stress versus rate of strain suggest that $n<1$, so this provides a physical test that the models must meet to be considered applicable. Another useful test of the models is the behavior of the rate of strain at r_c. In this case, the models predict very different behavior by construction. For the Herschel-Bulkley model the rate of strain is continuous at r_c, while for the power-law model there is an explicit discontinuity. Here, because of the discrete nature of the data, it is difficult to determine the continuity of the data by visual inspection. As we will show, other aspects of the fit clarify the nature of the transition.

There is an additional test of the applicability of the Herschel-Bulkley model: the behavior of r_c as a function of the external rotation rate Ω. Because the critical radius is set by the yield stress, $\sigma(r_c)=\tau_0$. From this, we can write $\sigma(r)=\tau_0 r_c^2/r^2$. Then as the rotation rate approaches zero, the rate of strain in Eq. (1) does as well, so $\sigma(r_i)$ approaches τ_0 and thus r_c approaches r_i.

The final question related to the choice of models is the use of these models in a discrete regime. By definition, both the Herschel-Bulkley model and the critical rate of the strain power-law model discussed here are continuum models. The key element of each is a single yield stress or critical rate of strain, respectively, that describes the properties of the foam in a continuum limit. It is difficult to modify the Herschel-Bulkley model to also describe a situation in which there is not a well-defined yield stress. However, if we consider the original general power-law model, it is useful as an *ad hoc* model in the case of discrete flow. As we saw, the solution for $v(r)$ in the case of a power-law fluid does not depend on $\dot{\gamma}_c$. Therefore, one would expect the fitting procedure to work equally well whether the system is exhibiting continuum or discrete behavior. However, the *results* can be used to distinguish between the two regimes based on the behavior of $\dot{\gamma}_c=\dot{\gamma}(r_c)$ and n. For a system in a well-defined continuum limit, these are expected to be material properties that are independent of the external rotation rate Ω. If one observes a strong dependence of these parameters on Ω, this would represent a breakdown of the continuum limit.

In summary, by considering two standard models for complex fluids (power-law fluid and Herschel-Bulkley models) we will be able to test two features of the flow. First, we will be able to distinguish between transitions that are continuous or discontinuous in the rate of strain. Second, we will be able to test for a transition from the continuum limit to discrete flow.

IV. RESULTS

Figure 1 illustrates the fitting procedure for the two models for a rotation rate of 0.09 s^{-1} and outer radius $R=9$ cm. The power-law fit is illustrated in Fig. 1(a), where the horizontal line indicates the rigid-body rotation. The fit is continued past the critical radius to highlight the fact that this model gives a nonzero critical rate of strain. This represents a discontinuous transition. In contrast, the fit in Fig. 1(b) is for the Herschel-Bulkley model and it is continuous by construction. From these fits alone, it is difficult to distinguish between these two models, especially at this rotation rate. Therefore, one needs to consider more carefully the parameters for the different models, as they are determined from the fits.

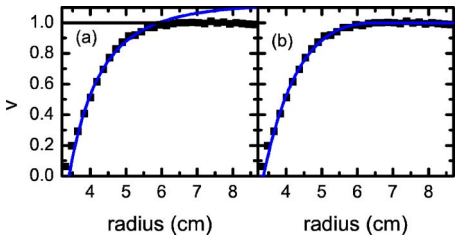

FIG. 1. (Color online) (a) A velocity profile (with $r_c=5.9$ cm) as a function of radial position for the system with outer radius of 9 cm and rotation rate of 0.09 s^{-1} (black symbols), with power-law fit where $n=0.515$ (blue line). (b) Same velocity profile (black symbols), with numeric fit to the Herschel-Bulkley model where $n=1.056$ (blue line).

Figure 2 provides a summary of the behavior of the critical radius as a function of system size and rotation rate. For comparison, we show both the calculation using the numerical fit to the Herschel-Bulkley model (open symbols) and the fit to a power-law and rigid-body coexistence model (solid symbols). The results for r_c based on each method are in reasonable agreement. This provided an important consistency check on both methods. It should be noted that once $r_c \approx R$, the various methods of determining r_c break down. To indicate where this occurs, we still plot r_c, but define it to be equivalent to R. In other words, $r_c=R$ is the condition that the entire sample be flowing.

Three important features are highlighted by this figure. First, the critical radius is roughly linear in the applied rota-

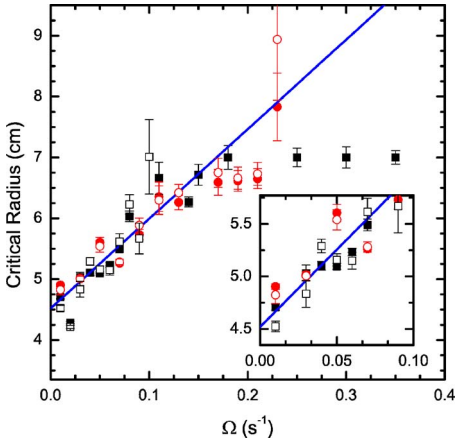

FIG. 2. (Color online) Comparison of the measured critical radius as a function of rotation rate for outer radii of 7 cm (black squares) and 9 cm (red circles). The open symbols correspond to calculation of r_c using a Herschel-Bulkley model, and the solid symbols correspond to calculating r_c assuming a power-law fluid coexisting with a solidlike state.

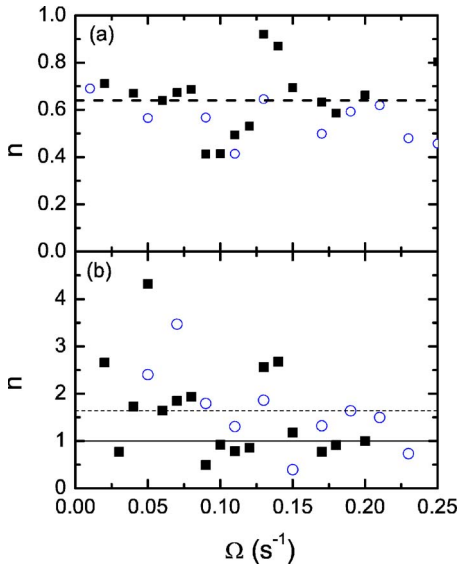

FIG. 3. (Color online) (a) The exponent n obtained from fitting the velocity curves to a power-law fluid coexisting with a solidlike state versus the external rotation rate for $R=7$ cm (black squares) and $R=9$ cm (blue circles). The dashed line is the median value. (b) The exponent n obtained from fitting the velocity curves to a Herschel-Bulkley model versus the external rotation rate for $R=7$ cm (black squares) and $R=9$ cm (blue circles). The dashed line is the median value of the exponents. The solid line is $n=1$.

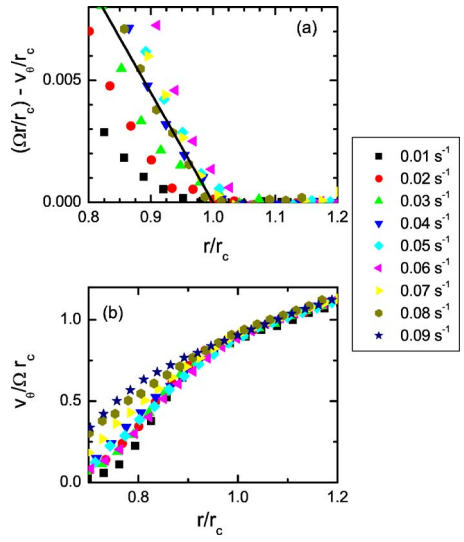

FIG. 4. (Color online) (a) Plot of the scaled velocity profiles $\tilde{v}=(\Omega r/r_c)-v_\theta/r_c$ versus r/r_c. Solid line is a guide to the eye. (b) Plot of $v_\theta/\Omega r_c$ versus r/r_c. Rates of strain are indicated in the legend. Both plots are for the system with an outer radius of 7 cm.

tion rate. (The straight line in the figure is a guide to the eye.) Second, for rotation rates less than 0.15 s^{-1}, changing the system size does not alter the location of the coexistence between the two regions. Once the critical radius is $r_c=7$ cm, in the $R=9$ cm system, the critical radius continues to increase with rotation rate. Finally, the critical radius approaches $r=4.5$ cm as Ω goes to zero. The fact that $r_c \rightarrow 4.5$ cm as $\Omega \rightarrow 0$ s^{-1} is the first evidence for the breakdown of the Herschel-Bulkley model, as discussed in Sec. III. As a further test of the behavior of r_c, we have considered two slower rates of strain: 1.0×10^{-3} s^{-1} and 3.0×10^{-3} s^{-1}. Due to the finite lifetime of the bubbles, the results for the velocity profiles were noisier at these extremely slow rates of strain than the data studied in detail in this paper. However, these profiles clearly exhibited a r_c that was close to but greater than 4.5 cm, consistent with the results reported in Fig. 2.

As discussed, the exponent n in both the Herschel-Bulkley model and the power-law model has physical significance. Figure 3 summarizes the values of n obtained in the various fits to the velocity profiles. Figure 3(a) is the results for the power-law model, with the $R=7$ cm and $R=9$ cm indicated by squares and circles, respectively. Figure 3(b) is the results for the Herschel-Bulkley model. The dashed line in each figure represents the median value for the exponents. There are two striking features in Fig. 3. First, neither fit provides a completely consistent value for n. However, the variation in the fits for the power-law model is smaller than the case of the Herschel-Bulkley model. Second, for the power-law fits, one consistently finds $n<1$, but in the majority of cases for Herschel-Bulkley model, $n>1$.

As the combination of Figs. 2 and 3 effectively rules out a Herschel-Bulkley model, it is necessary to further probe the applicability of the power-law model. This allows us to confirm whether or not the transition is truly discontinuous in the rate of strain and to look a transition from continuum to discrete flow. One approach is to consider the scaling of the velocity profiles. In this regard, there are two different scalings that are particularly useful. These are presented in Fig. 4, and these represent the central measurement of both the discontinuity in the transition and the transition from continuum to discrete flow. First, it is useful to directly test for the existence of a consistent critical rate of strain in the context of the power-law model. To do this, we follow the scaling arguments presented in Ref. [16]. Because we are rotating the outer cylinder, we first subtract out the rigid-body rotation. This gives a new transformed velocity $\tilde{v}=(\Omega r/r_c)-v_\theta/r_c$. In this form, $\tilde{v}=0$ at $r=r_c$. Therefore, rewriting the rate of strain in the form $\dot{\gamma}(r)=r\frac{d}{dr}\frac{v_\theta(r)}{r}=\frac{dv_\theta}{dr}-\frac{v_\theta}{r}$, we see that the slope of $\tilde{v}$ at $r=r_c$ is the critical rate of strain $\dot{\gamma}_c$. Therefore, if there is a single $\dot{\gamma}_c$ for the material, then $\tilde{v}$ as a function of r/r_c will collapse onto a single curve near $r/r_c=1$.

Figure 4(a) presents $\tilde{v}$ as a function of r/r_c in the range near r_c. This illustrates two features. First, for sufficiently high rates of strain, the data suggest a single value of $\dot{\gamma}_c$. The solid line indicates the slope that is approached by the data near r_c. However, this scaling breaks down below a critical value of the external rotation rate. Second, this form of the velocity highlights the discontinuity in the slope at the critical radius.

Given the apparent dependence of $\dot{\gamma}_c$ on Ω for slow rates of strain, it is useful to consider an alternative scaling of the data, given in Fig. 4(b). Here we plot $v_\theta/\Omega r_c$ as a function of r/r_c. For this case, we do not subtract the rigid-body behavior, which is apparent as the linear regime for $r/r_c>1$. This was done to confirm the consistent rigid-body behavior for all rotation rates. This scaling allows us to focus on the data for the slowest rotation rates, which did not scale in Fig.

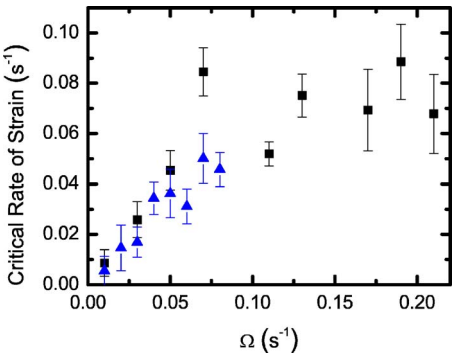

FIG. 5. (Color online) Critical rate of strain as a function of external rotation rate for $R=7$ cm (blue triangles) and $R=9$ cm (black squares).

4(a). In this case, we observe a collapse of the data for slow rates of strain, indicating a dependence of $\dot{\gamma}_c$ on Ω.

The final measurement of the discrete–continuum-flow transition is the direct measurement of $\dot{\gamma}_c$ as a function of Ω. This is plotted in Fig. 5. In this case, we fit the data for $\tilde{v}$ near r_c. Two features are illustrated by the data. First, for rotation rates below $\Omega=0.07\pm0.02$ s^{-1}, the critical rates of strain are dependent on the external rotation rate, but independent of the system size. Interestingly, the behavior is consistent with a linear dependence on Ω. This is strong evidence for the breakdown of any continuum description of the flow. Second, we observe a crossover to a regime in which $\dot{\gamma}_c$ is independent of Ω. This occurs for value of the external rotation above $\Omega=0.07\pm0.02$ s^{-1} and is consistent with the scaling of $\tilde{v}$ presented in Fig. 4(a). From these data, we find $\dot{\gamma}_c=0.07\pm0.01$ s^{-1}, where the error represents the standard deviation of the measured values of the critical rate of strain, for our bubble raft.

Given the possible breakdown of the continuum approximation, it is worth testing the short-time behavior and determining the approach to steady-state flow. This was done by considering a range of time intervals over which to compute the average bubble displacements and the corresponding average velocity profiles. For short enough time intervals, we were able to compute a histogram of the probability distribution for r_c. Here, the probability distribution is computed as follows. For each independent time interval, an average velocity profile is computed. As reported in Ref. [29], these profiles tend to be highly nonlinear, but there is a well-defined radius at which the profile deviates from a rigid-body rotation. This point is taken as the critical radius for that realization of the velocity profile. This is computed for each independent segment of data from a single run, and the probability distribution is generated from this set of data.

Figure 6 presents the probability distribution for the case of $\Omega=0.07$ s^{-1} and for four different time intervals used to compute the velocity profiles. As expected, the longer the time interval, the narrower the distribution. However, even for relatively short time intervals, the full width of the distribution is only on the order of 1 cm, or about three bubbles. As one increases the averaging time, the mean of the distribution remains constant to within 1%. Another way of considering the approach to steady state is illustrated in Fig. 7.

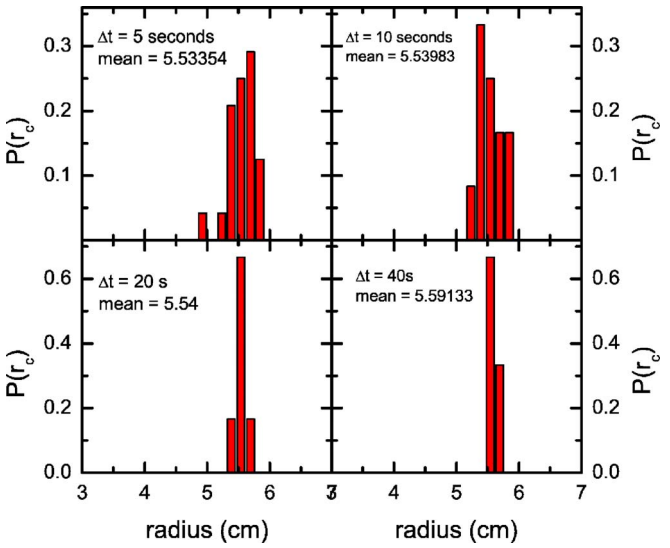

FIG. 6. (Color online) Probability distribution of measuring a particular value of r_c based on averaging the velocity over finite time intervals. Four different time intervals are illustrated for a rotation rate of 0.07 s^{-1} with $R=7$ cm. The time intervals and mean for each distribution are indicated in the figure.

This shows the computed critical radius for different sets of data using a fixed time interval. The plot illustrates that for time intervals greater than 50 s, the computed value of r_c does not change and that different measurements of r_c give the same value. (Due to the length of the run, there are two points for the $\Delta t=60$ s data, but one point for each of the larger values of Δt.)

V. DISCUSSION

The main focus of the measurements in this paper is to test carefully two aspects of the transition from solid to fluid behavior in a slowly driven foam: first, whether or not the transition is continuous or discontinuous in the rate of strain, and second, whether or not there is a transition from a discrete to a continuum flow regime. We used two standard models of complex fluids to interpret the experimental results: the Herschel-Bulkley model and a power-law model

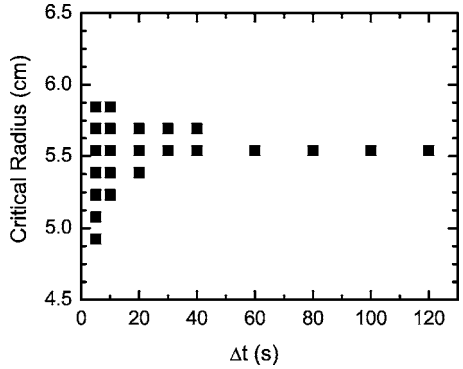

FIG. 7. Illustration of the convergence of the measured value of r_c as a function of the time interval over which the average velocity is computed is increased.

with a critical rate of strain. The evidence against the Herschel-Bulkley model suggests that it is better to understand the data in the context of the power-law model. In this context, we observe a clear discontinuity in the rate of strain at the transition and we observe the transition from discrete to continuous flow.

As discussed in Sec. III, the initial evidence against the Herschel-Bulkley model is the fact that r_c does not approach r_i as Ω goes to zero (see Fig. 2). Additional evidence against the model is the results for n presented in Fig. 3. The fact that we essentially always measure an $n>1$, in direct contrast to the measurements of the stress as a function of rate of strain, rules out the Herschel-Bulkley model. Finally, the scaling of the velocity in Fig. 4, which strongly suggests the existence of a discontinuity in the rate of strain, is behavior that is not possible in the context of the Herschel-Bulkley model. One might be concerned that despite this evidence, one appears to be able to fit the data to the Herschel-Bulkley model (as in Fig. 1). However, given the discrete nature of the data, the apparent fit to the Herschel-Bulkley model is most likely a result of the nonphysical values of n that are obtained.

In contrast to the Herschel-Bulkley model, the fits to the power-law model and the scaling in Fig. 4(a) strongly support the applicability of the power-law model and the corresponding discontinuity in the rate of strain. Therefore, it is reasonable to state that the localized flow in the bubble raft is best described by a coexistence of a power-law fluid and a solid region, with a discontinuity in rate of strain at the coexistence point. It raises the important question of the mechanism that determines the critical rate of strain. This will be the subject of future work. One promising direction is to use a parallel shear cell. In this case, one expects a uniform stress across the system and the global rate of strain is set by the boundaries. This can be used to further test the nature of the critical rates of strain. For example, in this case, it was determined to be $\dot{\gamma}_c=0.07\pm0.01$ s^{-1}.

An interesting open question is which features of the flow are determined by the details of the bubble raft. For example, how does $\dot{\gamma}_c$ depend on the specifics of the solution used to make the bubbles, the polydispersity, the bubble size, etc. Likewise, we observed that the value of n has potentially significant variation. For example, even though $n<1$ based on fits to the power-law model (Fig. 3), this exponent differs from past measurements in bubble rafts [3]. This difference is not surprising given that the details of the bubble rafts differed to some degree in terms of the exact nature of the bubble size distribution and the solutions used to make the bubbles. Also, once the flow is localized, it is not obvious how to connect the exponent from the velocity profile (which only fills part of the system) to the exponent measured from macroscopic stress measurements. This is especially true given that the exponent from the stress measurements is based on the high rotation rate limit. Finally, it should be noted that for the range of rotation rates studied here, the stress versus rate of strain curve is essentially flat (though extremely noisy). The flatness is consistent with past measurements for which the stress versus rate of strain at sufficiently slow external rotation rates is essentially flat. The noise is due to the fact that the velocity profiles converge more rapidly than the average stress measurements. Therefore, it was not possible to make a direct comparison between the local exponent from velocity curves and a more global exponent for stress versus rate of strain.

The transition from a continuum regime to a discrete regime is confirmed by the results presented in Figs. 4 and 5. Based on the scaling arguments from Ref. [16], the data in Fig. 4(a) are consistent with a single-continuum model based on a power-law fluid with a critical rate of strain for sufficiently high rotation rates. The breakdown of the scaling indicates the transition to the discrete regime. Directly plotting the critical rate of strain for each rotation rate and system size, we find that the transition between discrete and continuum behavior occurs at $\Omega=0.07\pm0.02$ s^{-1}. By considering two system sizes, we were also able to establish that the behavior is not dependent on system size. Conversely, we observe that the systems we have considered are large enough to exhibit behavior consistent with a continuum limit.

Using the results in Fig. 2 for the critical radius, a transition at $\Omega=0.07\pm0.02$ s^{-1} corresponds to a critical thickness for the flowing regime of approximately 10 bubbles. For comparison, the same transition is observed in three-dimensional bubbles for a thickness of 25 bubbles and a rotation rate of 0.3 s^{-1} [16]. At this point, it would be useful to consider both two- and three-dimensional models that capture this discontinuity to determine the source of the differences in these measurements. It might be dimensionality, but given the small differences, it is more likely related to details of the bubbles, such as bubble size, polydispersity, and surfactant composition. As current simulations only predict continuous transitions, work is first needed to elucidate the mechanism for the discontinuous transition.

It is worth commenting on the insights gained by consideration of the short-time behavior of the system. We focused on measurements of r_c as a function of the averaging time (as shown in Figs. 6 and 7). This was useful because it provided confirmation that our results represent the steady state of the system. It will be interesting in the future to compare the fluctuations in r_c in this system to other fluctuating transitions between regions with different types of flow such as those that have been observed in other complex fluids [6,7].

Finally, though we have analyzed our results within the context of relatively "traditional" constitutive relations between stress and rate of strain, it is very useful to think of the results in the context of a proposed jamming phase diagram [30]. Essentially, the jamming transition refers to the transition from solidlike to fluidlike behavior (or vice versa) in a system as a function of density, temperature, or externally applied stress. Of particular interest is the correspondence between transitions due to a critical stress and the more familiar transitions (such as the glass transition) as a function of temperature and density [31]. By connecting the coexistence of a flowing and stationary state with the concepts of the jamming transition, one may be better able to understand the mechanism that produces both the coexistence and the discontinuity in rate of strain. Physically, the coexistence of a flowing and stationary state is very natural in the context of phase transitions, especially a coexistence with a discontinuity. The existence of a discontinuity presents a natural analog

to a first-order phase transition. Therefore, the jamming transition is a natural context within which to explore the observed behavior in more detail.

ACKNOWLEDGMENTS

This work was supported by Department of Energy Grant No. DE-FG02-03ED46071. The authors thank K. Krishan and P. Coussot for useful discussions.

APPENDIX

In this appendix, we present some of the details of the derivation of the velocity profiles. The derivation of the profile for the power-law fluid is standard [28]. One combines the general expression for the stress in a Couette geometry and the relation between the stress and the rate of strain,

$$\sigma(r) = C/r^2 = \mu(\dot{\gamma}/\dot{\gamma}_c)^n, \tag{A1}$$

and combining all the constants, this simplifies to

$$\dot{\gamma} = D/r^{2/n}. \tag{A2}$$

Using the definition of $\dot{\gamma}$, one gets

$$\dot{\gamma} = r\frac{d}{dr}\frac{v_\theta(r)}{r} = D/r^{2/n}, \tag{A3}$$

which can be directly integrated to get (dividing by Ω)

$$\frac{v_\theta(r)}{\Omega r} \equiv v(r) = \frac{A}{r^{2/n}} - B. \tag{A4}$$

As given in Sec. III, the boundary conditions determine A and B in terms of n, r_c, and r_i.

The derivation for the Herschel-Bulkley model follows along similar lines, only now it is useful to explicitly write out the constant in the stress relation

$$\sigma(r) = C/r^2 = \sigma(r_i)r_i^2/r^2 = \tau_0 r_c^2/r^2. \tag{A5}$$

Notice that there are two equivalent ways to write the constant because it is based on the equivalence of torques in the radial direction [28]. Again, we equate this expression for the stress with the constitutive relation

$$\tau_0 r_c^2/r^2 = \tau_0 + \mu\dot{\gamma}^n. \tag{A6}$$

This gives

$$\dot{\gamma} = (\tau_0/\mu)^{1/n}[r_c^2/r^2 - 1]^{1/n}. \tag{A7}$$

In this case, integration does not result in an analytic expression; instead, we get

$$\frac{v_\theta}{r} = \left(\frac{\tau_0}{\mu}\right)^{1/n}\int_{r_i}^{r}\frac{1}{\rho}\left[\left(\frac{r_c}{\rho}\right)^2 - 1\right]^{1/n} d\rho + C. \tag{A8}$$

Here the constant $C=0$ because $v_\theta/r=0$ at $r=r_i$. Requiring solid-body rotation $v_\theta=\Omega r$ at $r=r_c$ gives

$$\frac{v_\theta(r_c)}{\Omega r_c} = 1 = \frac{1}{\Omega}\left(\frac{\tau_0}{\mu}\right)^{1/n}\int_{r_i}^{r_c}\frac{1}{\rho}\left[\left(\frac{r_c}{\rho}\right)^2 - 1\right]^{1/n} d\rho. \tag{A9}$$

Therefore, converting to $v(r) \equiv v_\theta(r)/(\Omega r)$,

$$v(r) = \frac{1}{N}\int_{r_i}^{r}\frac{1}{\rho}\left[\left(\frac{r_c}{\rho}\right)^2 - 1\right]^{1/n} d\rho, \tag{A10}$$

where

$$N = \int_{r_i}^{r_c}\frac{1}{\rho}\left[\left(\frac{r_c}{\rho}\right)^2 - 1\right]^{1/n} d\rho.$$

This is a useful form for numerically fitting the data by approximating the integral.

[1] Various books cover both the modeling and experimental measurement of yield stress materials and complex fluids in general. Two examples are R. B. Bird, R. C. Armstrong, and O. Hassage, *Dynamics of Polymer Liquids* (Wiley, New York, 1977) and C. Macosko, *Rheology Principles, Measurements, and Applications* (VCH, New York, 1994).
[2] G. Debrégeas, H. Tabuteau, and J. M. di Meglio, Phys. Rev. Lett. **87**, 178305 (2001).
[3] J. Lauridsen, G. Chanan, and M. Dennin, Phys. Rev. Lett. **93**, 018303 (2004).
[4] P. Coussot, J. S. Raynaud, F. Bertrand, P. Moucheront, J. P. Guilbaud, H. T. Huynh, S. Jarny, and D. Lesueur, Phys. Rev. Lett. **88**, 218301 (2002).
[5] J.-B. Salmon, A. Colin, S. Manneville, and F. Molino, Phys. Rev. Lett. **90**, 228303 (2003).
[6] S. Lerouge, M. Argentina, and J. P. Decruppe, Phys. Rev. Lett. **96**, 088301 (2006).
[7] J.-B. Salmon, S. Manneville, and A. Colin, Phys. Rev. E **68**, 051504 (2003).
[8] J.-B. Salmon, S. Manneville, and A. Colin, Phys. Rev. E **68**, 051503 (2003).
[9] D. Howell, R. P. Behringer, and C. Veje, Phys. Rev. Lett. **82**, 5241 (1999).
[10] W. Losert, L. Bocquet, T. C. Lubensky, and J. P. Gollub, Phys. Rev. Lett. **85**, 1428 (2000).
[11] D. M. Mueth, G. F. Debregeas, G. S. Karczmar, P. J. Eng, S. R. Nagel, and H. M. Jaeger, Nature (London) **406**, 385 (2000).
[12] N. Huang, G. Ovarlez, F. Bertrand, S. Rodts, P. Coussot, and D. Bonn, Phys. Rev. Lett. **94**, 028301 (2005).
[13] A. D. Gopal and D. J. Durian, J. Colloid Interface Sci. **213**, 169 (1999).
[14] J. Lauridsen, M. Twardos, and M. Dennin, Phys. Rev. Lett. **89**, 098303 (2002).
[15] F. Rouyer, S. Cohen-Addad, M. Vignes-Adler, and R. Höhler, Phys. Rev. E **67**, 021405 (2003).
[16] S. Rodts, J. C. Baudez, and P. Coussot, Europhys. Lett. **69**, 636 (2005).
[17] Y. Wang, K. Krishan, and M. Dennin, Phys. Rev. E **73**, 031401

(2006).
[18] D. Weaire, E. Janiaud, and S. Hutzler, e-print cond-mat/0602021.
[19] A. Kabla and G. Debrégeas, Phys. Rev. Lett. **90**, 258303 (2003).
[20] F. Varnik, L. Bocquet, J.-L. Barrat, and L. Berthier, Phys. Rev. Lett. **90**, 095702 (2003).
[21] N. Xu, C. S. O'Hern, and L. Kondic, Phys. Rev. Lett. **94**, 016001 (2005).
[22] N. Xu, C. S. O'Hern, and L. Kondic, Phys. Rev. E **72**, 041504 (2005).
[23] L. Bragg and W. M. Lomer, Proc. R. Soc. London, Ser. A **196**, 171 (1949).
[24] A. S. Argon and H. Y. Kuo, Mater. Sci. Eng. **39**, 101 (1979).
[25] R. S. Ghaskadvi and M. Dennin, Rev. Sci. Instrum. **69**, 3568 (1998).
[26] E. Pratt and M. Dennin, Phys. Rev. E **67**, 051402 (2003).
[27] M. Twardos and M. Dennin, Phys. Rev. E **71**, 061401 (2005).
[28] R. B. Bird, R. C. Armstrong, and O. Hassager, *Dynamics of Polymer Liquids* (Wiley, New York, 1977).
[29] M. Dennin, Phys. Rev. E **70**, 041406 (2004).
[30] A. J. Liu and S. R. Nagel, Nature (London) **396**, 21 (1998).
[31] *Jamming and Rheology*, edited by A. J. Liu and S. R. Nagel (Taylor & Francis, London, 2001).